

# CrystEngComm

Accepted Manuscript

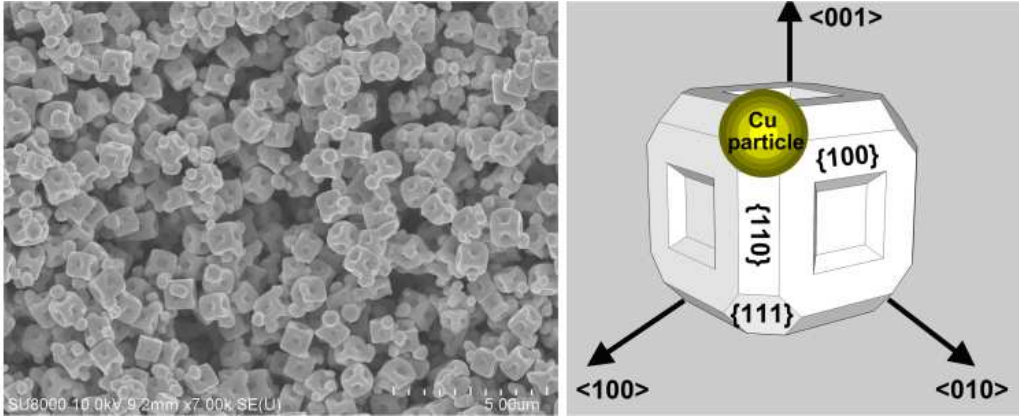


This is an *Accepted Manuscript*, which has been through the Royal Society of Chemistry peer review process and has been accepted for publication.

*Accepted Manuscripts* are published online shortly after acceptance, before technical editing, formatting and proof reading. Using this free service, authors can make their results available to the community, in citable form, before we publish the edited article. We will replace this *Accepted Manuscript* with the edited and formatted *Advance Article* as soon as it is available.

You can find more information about *Accepted Manuscripts* in the [Information for Authors](#).

Please note that technical editing may introduce minor changes to the text and/or graphics, which may alter content. The journal's standard [Terms & Conditions](#) and the [Ethical guidelines](#) still apply. In no event shall the Royal Society of Chemistry be held responsible for any errors or omissions in this *Accepted Manuscript* or any consequences arising from the use of any information it contains.



## ARTICLE

# A facile one-pot synthesis of Cu-Cu<sub>2</sub>O concave cube hybrid architectures

Cite this: DOI: 10.1039/x0xx00000x

Caijin Huang,<sup>a</sup> Zhen Long,<sup>b</sup> Masahiro Miyauchi,<sup>\*c</sup> Xiaoqing Qiu<sup>\*a</sup>Received 00th January 2014,  
Accepted 00th January 2014

DOI: 10.1039/x0xx00000x

[www.rsc.org/](http://www.rsc.org/)

Novel Cu-Cu<sub>2</sub>O concave cube hybrid architectures are prepared via a facile solution method. The spherical Cu particle is intimately attached to the surfaces of the truncated Cu<sub>2</sub>O cube that is enclosed by {110} edges, {111} corners, and {100} facets with truncated pyramid-like pits to form the hybrid architecture. The formation of the concave hybrid architectures involves over-reduction and caramelization of glucose under strong alkaline condition. As an anode, the hybrid architectures show superior electrochemical performance for lithium-ion batteries to truncated Cu<sub>2</sub>O cubes and irregular Cu<sub>2</sub>O crystals.

## Introduction

Multicomponent composites comprising different type materials represent a new approach towards materials design.<sup>1</sup> Such composites offer novel properties beyond the individual components, and are quite attractive due to their tailorable structures via hybridization. Metal-semiconductor hybrid structures, especially, have attracted much attention, because of their potential applications in diluted magnetic semiconductors, optoelectronic devices, sensors, photocatalysis, and lithium-ion batteries.<sup>2-9</sup> However, Compared with the significant progress achieved in the single-component nano/microcrystals synthesis,<sup>10-13</sup> the formation of well-controllable hybrid structures has been lingering for behind. The most strategies available to synthesize metal-semiconductor hybrid structures often require multistep procedures, which generally involve the sequential deposition or epitaxial growth of a second material on the surfaces of presynthesized nano/microcrystals in harsh conditions.<sup>1,5</sup> It remains a great challenge to develop a simple and effective method for one-pot solution synthesis of the metal-semiconductor hybrid structures.<sup>14</sup>

Cuprous oxide (Cu<sub>2</sub>O), an important p-type semiconductor with a direct band gap of 2.17 eV, has attracted great interests due to its unique properties and wide applications in catalysis,<sup>15,16</sup> biocide,<sup>7,17</sup> gas sensors,<sup>18</sup> solar energy photovoltaics,<sup>19</sup> and lithium-ion batteries.<sup>20</sup> Moreover, Cu<sub>2</sub>O nano/microstructures with a diversity of well-defined morphologies have been successfully synthesized using various methods, including cubes, octahedrons, spheres, stars and hollow structures.<sup>21-24</sup> Following the shape modulation of Cu<sub>2</sub>O structures, the hybrid combination of Cu<sub>2</sub>O nano/microstructures with the metal presents interesting fundamental issues related to the chemistry of the process, and concerning the improved properties in the metal-semiconductor

hybrid structures compared to each component. Recently, a series of hybrid structures with metal core and Cu<sub>2</sub>O shell were obtained by growing Cu<sub>2</sub>O on the metal seed beforehand such as Pt, Au, Pd, and Ag.<sup>25-28</sup> It has been reported that significant enhancement of electrical property and expanded plasmonic tenability can be achieved in the Au-Cu<sub>2</sub>O core-shell structures.<sup>26,29</sup> In addition, it has also been demonstrated that discharge capacity of Cu<sub>2</sub>O was much improved by the hybridization with conductive carbon nanotubes.<sup>30</sup> It is well known that metal copper is one of the best conductors of both heat and electricity, which has a key role to play in many reactions and energy efficiency.<sup>31</sup> Therefore, much effort has been devoted to combine the advantageous properties of Cu with semiconductors.<sup>14,32-34</sup> For example, Wang *et al.*, found that a minor amount of metal Cu led to an obvious enhancement of conductivity of the Cu/Cu<sub>2</sub>O hollow microspheres.<sup>35</sup> However, since Cu belongs to the light transition metal, the oxides of Cu normally form on the surfaces of copper particles,<sup>18</sup> accounting for that the most developed Cu-based hybrid structures with the Cu core and semiconductor shell rather than the Cu-decorated semiconductors.<sup>32,36</sup> To maximize the synergy effect, it is highly desirable to synthesize structurally well-defined metal-decorated semiconductor particles by exposing the active sites of both metal component and semiconductor component as well as the interface of hybrid structures,<sup>8,37</sup> particularly with respect to large-scale preparation and shape monodispersity and uniformity.

Herein, we report an efficient gram-scale synthesis of Cu-Cu<sub>2</sub>O concave cube hybrid architectures by a facile one-pot solution process. The highly monodisperse Cu<sub>2</sub>O cubes were decorated with Cu particles originated from the over-reduction of Cu(II) with glucose in strong base solution. These Cu<sub>2</sub>O cubes and Cu-Cu<sub>2</sub>O concave cube hybrid architectures were used as anode

materials in lithium ion batteries. It was found that the electrodes containing Cu-Cu<sub>2</sub>O concave cube hybrid architectures delivered a reversible capacity of 241 mAhg<sup>-1</sup> with a high Coulombic efficiency of 99% after the 50th cycle.

## Experimental

All the chemicals were analytic grade reagents and used as received without further purification. The scheme of the experimental procedure is presented in Fig. S1. In a typical synthesis, 0.01 mol CuCl<sub>2</sub>·2H<sub>2</sub>O was firstly dissolved in 100 mL distilled water using a glass flask with stirring at 60 °C to form a clear green solution. 20 mL of NaOH water solution (0.1 mol) was added drop-wise into the above CuCl<sub>2</sub> solution. The resulting dark suspension was stirred with a magnetic stirrer at 60 °C for 20 min. Then, 30 mL of glucose solution (0.01 mol) was added as a reducing agent. The reaction was kept at 60 °C. After a desired period reaction time, the brick red products were collected by filtrating, washed thoroughly with distilled water, and dried in air at ambient condition. For comparison, the control experiment was also performed under N<sub>2</sub> protection for 4 h after the addition of glucose at 60 °C.

The structural characteristics of the obtained products were measured by X-ray diffraction (XRD) at room temperature on a Rigaku SmartLab 2080B202 diffractometer. The data were collected from 2θ = 10–70° in a step-scan mode. The morphologies of the samples were investigated by a field-emission scanning electron microscopy (SEM) using a JEOL JSM-6700 apparatus and transition electron microscopy (TEM) on a Hitachi HF-2000 instrument under an acceleration voltage of 200 kV. The absorption spectra of the thin were recorded using a UV-2550 spectrophotometer (Shimadzu).

The anode materials were fabricated by mixing active materials (Cu-Cu<sub>2</sub>O hybrid architectures or pure Cu<sub>2</sub>O), acetylene black, and PVDF at a weight ratio of 60:20:20, respectively, using N-methylpyrrolidone (NMP) as a solvent. The resulting slurries were cast onto copper foil, and then dried at 120 °C under vacuum for 12 h to remove the solvent. The electrode foils were then cut into disks (12 mm in diameter). CR2025 coin-type cells were assembled in an argon-filled glovebox (H<sub>2</sub>O and O<sub>2</sub> concentration < 1 ppm) by using metal lithium foil as the counter electrode, 1 M LiPF<sub>6</sub> in a 1:1:1 (in volume) mixture of ethylene carbonate (EC), ethyl methyl carbonate (EMC), and dimethyl carbonate (DMC) as electrolyte, and porous polypropylene film separator. The cells were charged and discharged galvanostatically using a battery tester (Shenzhen Neware Electronic Ltd., China) in a potential range between 0.01 and 3.0 V. The electrochemical impedance spectroscopy (EIS) were measured using an electrochemical workstation (CHI660B).

## Results and discussion

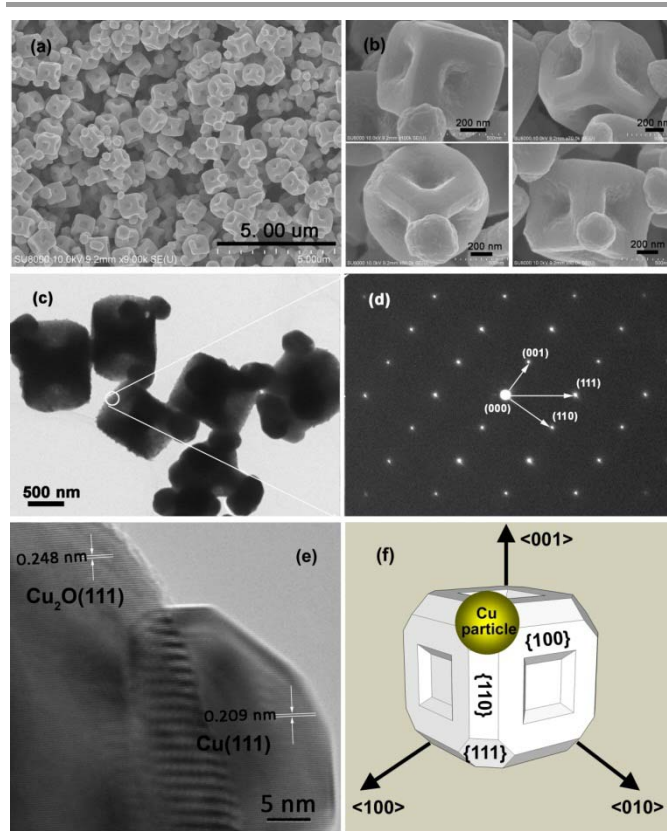


**Fig. 1** (a) Low-magnification SEM image of Cu-Cu<sub>2</sub>O concave cube hybrid architectures obtained from the reaction mixture after 30 min reaction with glucose at 60 °C. (b) A gallery of individual hybrid architecture. (c) The corresponding TEM image. (d) SAED pattern. (e) HRTEM image. (f) The ideal model of a Cu-Cu<sub>2</sub>O concave cube hybrid architecture.

Well-developed Cu-Cu<sub>2</sub>O concave cube hybrid architectures were obtained on a large scale from the reaction mixture after 30 min reaction with glucose at 60 °C. Field-emission scanning electron microscopy (SEM) images provided insight into the morphological features of the hybrid architectures. As shown in Fig. 1a, there exist two types of particles: one is spherical particles, and the other is truncated cubes with pits in facets. The truncated cubes are monodisperse and rather uniform in edge length of 980 nm. The high magnification SEM images of single hybrid structure are depicted as a gallery in Fig. 1b. As can be clearly seen, the truncated pyramid-like pits are located at the centre of six {100} facets of the truncated cubes. The spherical particles are intimately attached to the corner or the edge of the truncated concave cubes. The average size of spherical particles is about 390 nm. Notably, Most of the hybrid architectures are composed of one truncated concave cube and one spherical particle, while more than one spherical particle per cube is also observed. Consistent with the SEM observations, transmission electron microscopy (TEM) images (Fig. 1c) show the hybrid architectures are comprised of spherical particles and cubes. The concavity features can be easily distinguished with a contrast. Unlike the conventional hollow structures such as nanocages and nanoframes,<sup>38</sup> the concave holes do not go through the cubes. The corresponding

selected area electron diffraction (SAED) pattern (Fig. 1d) taken on the edge of truncated cubes shows that they are perfect  $\text{Cu}_2\text{O}$  single crystals, in which the spots reveals that the edges of truncated  $\text{Cu}_2\text{O}$  cubes exclusively exposing  $\{110\}$  planes. A high-magnification TEM image of individual hybrid structure (Fig. 1e) shows that the regular spacing of the lattice planes for the spherical particle is 0.209 nm, in good agreement with the (111) lattice spacing of metal Cu, while the interplanar spacing of the truncated cubes is 0.248 nm, which is compatible with that of  $\text{Cu}_2\text{O}$  (111) planes, the corner facet of the truncated cubes. Additionally, as shown in Fig. 1e, the hybrid junction between the Cu metal particles and  $\text{Cu}_2\text{O}$  truncated cubes is evidenced by intimate contact of the clear lattice fringes, a property that might be beneficial for the improved electrochemical performance for lithium ion battery. The location of Cu particles on the edge and corners of  $\text{Cu}_2\text{O}$  cubes is probably due to the structural similarity and lattice match between the (111) lattice of Cu spheres and the  $\text{Cu}_2\text{O}$  (111) planes of the cube corners. An ideal model of our novel hybrid architecture is illustrated in Fig. 1f. The spherical Cu particle is attached to the surfaces of the truncated  $\text{Cu}_2\text{O}$  cube that is enclosed by  $\{110\}$  edges,  $\{111\}$  corners, and  $\{100\}$  facets with truncated pyramid-like pits.

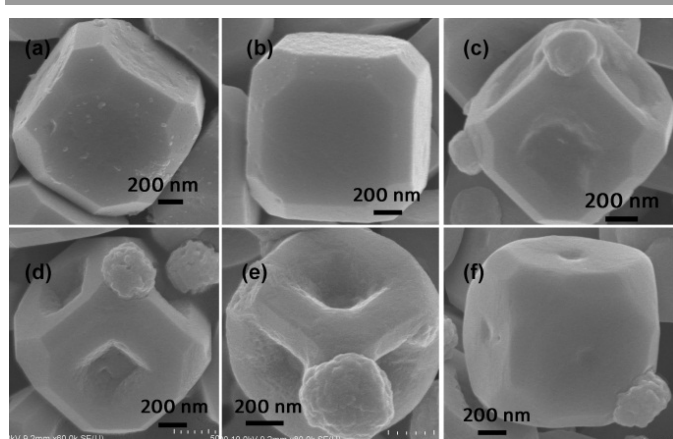


**Fig. 2** SEM images of samples obtained from the reaction mixture after reaction with glucose at 60 °C for various time. (a) 3 min. (b) 5 min. (c) 10 min. (d) 15 min. (e) 30 min. (f) 60 min.

To clarify the formation mechanism of the hybrid architecture, we examined its composition and morphological evolution process with the reaction time by SEM observations in combination with the x-ray diffraction (XRD) technique. Generally, various copper precursors can be reduced by glucose to form  $\text{Cu}_2\text{O}$  precipitates, where the copper precursor is a key parameter influencing size and shape of  $\text{Cu}_2\text{O}$  crystals.<sup>39</sup> For full understanding the subsequent hybrid structure growth, the black precursor in our experimental is therefore collected prior to glucose reduction (Fig. S1 and S3, Supporting Information). The XRD pattern (Fig. S2) suggests that the precursor is actually pure CuO with a monoclinic crystal structure (JCPDS No. 89-5899). SEM images (Fig. S3) shows the CuO precursor consists of many nanosheet-like grains. Remarkably, these nanosheet-like CuO grains were quickly transformed to

uniform and regular truncated cubes, when the reductant glucose was introduced into the reaction mixture. As shown in Fig. 2a and Fig. S4, highly monodisperse truncated cubes were obtained on a large scale after reaction with glucose at 60 °C for 3 min. The mean particle size of the cubes estimated from the SEM analysis is about 1.02  $\mu\text{m}$ , a value that is compatible to those of truncated concave cubes component in the above hybrid architectures. The related XRD of such truncated cubes shows a typical reflection pattern of pure  $\text{Cu}_2\text{O}$  crystals (Fig. S5, JCPDS No. 77-0199). According to *fcc* structure of  $\text{Cu}_2\text{O}$  crystals, the truncated cubes with well-defined edges and surfaces actually have 26 facets, including 6  $\{100\}$  basal planes, 12  $\{110\}$  edge surfaces, and 8  $\{111\}$  corner surfaces (Fig. 2a and Fig. S4). The crystal structure and morphology of the cubes remain nearly unchanged when the reaction time was prolonged to 5 min (Fig. 2b, Fig. S5 and Fig. S6). Interestingly, as the reaction time reached 10 min, shallow pits formed in the middle of the basal  $\{100\}$  planes (Fig. 2c and Fig. S7). Simultaneously, the truncated  $\text{Cu}_2\text{O}$  cubes were decorated by small particles on the  $\{111\}$  corner, which have been demonstrated to be metallic Cu particles by XRD analysis (Fig. S5). When the reaction time was extended to 15 min, as indicated in Fig. 2d and Fig. S8, the sizes of Cu particles and pits increased, and the XRD diffraction peaks from metallic Cu become stronger in intensity (Fig. S5). When the reaction time was prolonged to 30 min, well-developed Cu- $\text{Cu}_2\text{O}$  concave cubes hybrid architectures were achieved, as displayed in Fig. 1. The relative metallic Cu content in the hybrid architectures is calculated to be 27.6 wt% by Rietveld-based XRD analysis (Fig. S5b). Surprisingly, the sizes of these Cu particles and the pits reduced as further prolonging the reaction time to 1 h (Fig. 2e and Fig. S9). The vast majority of the Cu particles and pits diminished, when the reaction time was extended to 2 h (Fig. S10). Finally, the pure  $\text{Cu}_2\text{O}$  crystals with irregular shape, a common member to the  $\text{Cu}_2\text{O}$  family, were obtained (Fig. S11), when the reaction time was increased to 4 h. These experimental observations demonstrate that Cu- $\text{Cu}_2\text{O}$  concave cubes hybrid architectures can be successfully obtained by simply tuning the reaction time, and provide new insights into the over-reduction of Cu(II) in alkaline system by glucose.

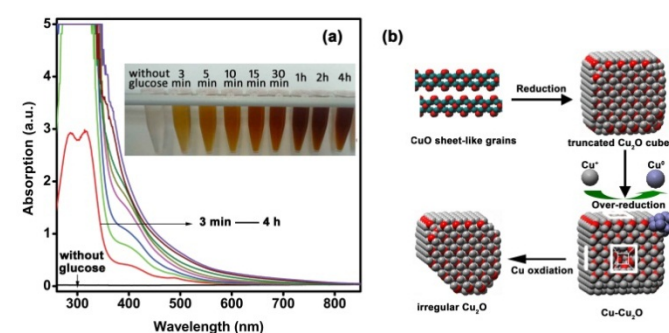


**Fig. 3** UV-visible spectra of the residual solution accompanying the evolution of Cu- $\text{Cu}_2\text{O}$  hybrid architectures in composition and morphologies; Inset: the corresponding photographs. (b) Schematic illustration of the formation mechanism and the shape-evolution processes.

Unlike in the case of strong reducing agent such as hydrazine hydrate,<sup>40</sup> over-reduction of copper oxide involving glucose is little reported. To understand the total reaction, the UV-visible spectra of the residual solutions collected at different stages of the formation process is explored. The photographs of the residual solutions (Inset of Fig. 3a) show the time-course of color changes accompanying the evolution of Cu-Cu<sub>2</sub>O hybrid architectures in composition and morphologies (Fig. 2). The residual solution turns slight yellow, then orange and finally brown. The corresponding UV-visible spectra are given in Fig. 3a. The residual solution before adding glucose is almost completely transparent without any absorption above 250 nm, suggesting that negligible Cu(II) species in the residual solution.<sup>41</sup> After the reaction with glucose for 3 min, the residual solution exhibits two well-resolved diagnostic peaks of glucose<sup>42,43</sup> around 285 and 316 nm as well as a set of weak peaks above 400 nm, indicating the survival of reductant glucose in the reaction system. As the reaction time prolonging, the set of peaks above 400 nm becomes stronger, and an evident red-shift of the absorption band edge is observed. The time evolution of the optical absorption edge of the residual solution is similar to the well-known caramelization of sugar.<sup>44</sup> The caramelization process involves condensation, isomerization, dehydration, fragmentation, and polymerization reactions to various non-reductive high molecular weight coloring components under high temperature.<sup>45,46</sup> It is also reported that the hot strong alkaline condition can induce the caramelization.<sup>47</sup> In our study, the considerable amount of excess NaOH gives a strong alkaline condition. It is, therefore, believed that the color changes in our study originated from the caramelization of glucose. Thus, based on the above results, we propose a three-stage growth mechanism for the Cu-Cu<sub>2</sub>O hybrid architectures evolution. That is, nanosheet-like CuO grains were firstly fast reduced by glucose to form truncated Cu<sub>2</sub>O cubes. As discussed above, the truncated Cu<sub>2</sub>O cubes have 6 {100} basal planes. Among the {100}, {110}, and {111} low-index surfaces of Cu<sub>2</sub>O, copper atoms in {100} surfaces undergo a drastic surface reconstruction, resulting in the outermost surface copper atoms to form Cu-Cu dimers.<sup>48</sup> These Cu-Cu dimers are then readily over-reduced by the survival of glucose to form the Cu-Cu<sub>2</sub>O concave cubes hybrid architectures. Along with the caramelization of glucose, the reductibility of the reaction system gradually decreased, thereby ceasing the over-reduction and prohibiting the formation of the conventional hollow structures. On the other hand, the oxidation of metallic Cu particles can occur involving the oxygen under the strong alkaline condition.<sup>49</sup> To further understand the pits feature elimination as the reaction time extending, a control experiment under N<sub>2</sub> condition was preformed. As shown in Figure S12, the metallic Cu peaks were evidently observed when the reaction time was even extended to 4 h under N<sub>2</sub> protection. However, the only pure Cu<sub>2</sub>O samples were obtained when the experiment was conducted in air for 4 h. The SEM observations (Figure S13) reveal that N<sub>2</sub> protection can maintain the morphology of Cu-Cu<sub>2</sub>O concave cubes hybrid architectures even the reaction was extended to 4h,

which further confirmed that the oxidation of Cu spheres was involved in the pits feature elimination as the prolongation of the reaction. As a consequence, the Cu particles and the pits in the {100} surfaces slowly disappeared with the further prolongation of the reaction, leading to the final formation of irregular Cu<sub>2</sub>O crystals. The proposed the reaction process and the formation and evolution mechanism of Cu-Cu<sub>2</sub>O hybrid architectures can be schematically illustrated in Fig. 3b.

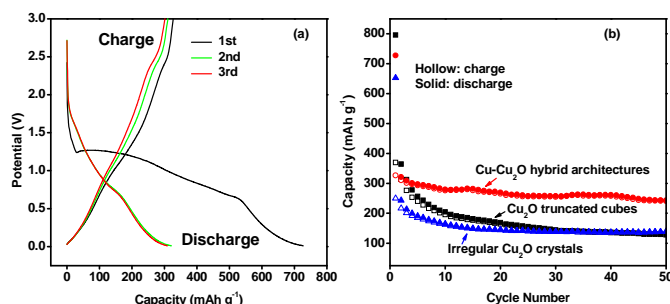


**Fig. 4** (a) The discharge-charge curves for Cu-Cu<sub>2</sub>O hybrid architectures. (b) Cycling performance of truncated Cu<sub>2</sub>O cubes, irregular Cu<sub>2</sub>O crystals, and Cu-Cu<sub>2</sub>O hybrid architectures.

Since the pioneer work of Tarascon's group,<sup>20</sup> transition-metal oxides have become a promising class of anode materials for lithium ion batteries.<sup>50,51</sup> However, poor electronic conductivity of metal oxides leads to the low coulombic efficiencies and cycling stability and restricts their application in high-performance lithium ion batteries.<sup>52</sup> Based on the above discussion, the Cu-Cu<sub>2</sub>O hybrid architectures with the conductive Cu particles on the corners were successfully achieved by controlling the over-reduction of glucose. Consequently, we next examined the electrochemical property as anode materials for Li-ion batteries. Electrochemical property of Cu-Cu<sub>2</sub>O hybrid architectures was evaluated by galvanostatic charge-discharge cycling at a current density of 380 mA g<sup>-1</sup> (about 1C), as shown in Fig. 4. For comparison, the electrochemical properties for Cu<sub>2</sub>O truncated cubes and irregular Cu<sub>2</sub>O crystals measured under the same electrochemical conditions were also measured. Fig. 4a gives the charge-discharge curves of the electrode fabricated using the Cu-Cu<sub>2</sub>O hybrid architectures in the initial three cycles. In the first discharge step, Cu-Cu<sub>2</sub>O electrode show an abrupt drop in potential down to about 1.2 V, followed by a long voltage plateau between 1.2 and 0.8 V and a tilt curve down to the cutoff voltage of 0.01 V, which are typical characteristics of voltage trends for Cu<sub>2</sub>O film<sup>53</sup> and also the same with those of Cu<sub>2</sub>O truncated cubes and irregular Cu<sub>2</sub>O crystals (Supporting Information, Fig. S14). The long voltage plateau between 1.2 and 0.8 V corresponds to the electrode reaction:<sup>30</sup>  $\text{Cu}_2\text{O} + 2\text{Li}^+ + 2\text{e}^- \leftrightarrow \text{Li}_2\text{O} + 2\text{Cu}$ , as confirmed by ex situ XRD pattern of the electrode after the charge-discharge cycling (Fig. S15). The first discharge and charge capacities are 728 and 327 mAh g<sup>-1</sup> for Cu-Cu<sub>2</sub>O electrode. Compared to the theoretical capacity of Cu<sub>2</sub>O (375 mAh g<sup>-1</sup>), the initial extra discharge capacity is generally attributed to surface phenomena such as the

decomposition of electrolyte accompanying the formation of the solid electrolyte interface (SEI) layer, possibly interfacial lithium storage, as well as efficient transport of lithium ions granted by the hybrid structure. The first charge capacity is much less than the first discharge capacity, which may result from the incomplete conversion reaction and irreversible lithium loss due to the formation of SEI layer.<sup>53</sup>

Fig. 4b shows the cycling performance for the electrodes of Cu-Cu<sub>2</sub>O hybrid architectures, Cu<sub>2</sub>O truncated cubes, and irregular Cu<sub>2</sub>O crystals. It is seen that Cu-Cu<sub>2</sub>O electrodes exhibit a much better electrochemical performance compared to the Cu<sub>2</sub>O truncated cubes or irregular Cu<sub>2</sub>O crystals. After 50 cycles, the reversible capacity of Cu<sub>2</sub>O truncated cubes rapidly dropped from 799 to 129 mAh g<sup>-1</sup>, while irregular Cu<sub>2</sub>O crystals only delivered a reversible capacity of 140 mAh g<sup>-1</sup>. Comparatively, Cu-Cu<sub>2</sub>O hybrid architectures still delivered a reversible capacity of 241 mAh g<sup>-1</sup> with a high Coulombic efficiency of 99% after the 50th cycle. In order to understand the better electrochemical properties of Cu-Cu<sub>2</sub>O hybrids, electrochemical impedance spectroscopy (EIS) was carried out. As shown in Figure S16, all Nyquist plots show a semicircle together with an inclined line, which is associated with the SEI film resistance and charge transfer kinetics between the electrode-electrolyte interface.<sup>53</sup> The semicircle of Cu-Cu<sub>2</sub>O hybrids is much smaller than that of pure Cu<sub>2</sub>O, indicating that Cu component in the hybrids can efficiently improve the electronic conductivity. Therefore, the superior electrochemical performance for Cu-Cu<sub>2</sub>O concave cube hybrid architectures may be due to three factors: 1) the pit structure of the hybrid architectures leads to larger quantity of active sites for the reaction of Li ions that is necessary for higher capacity;<sup>54</sup> 2) the special concave structure can provide buffer space to accommodate the volume change and thus the strain associated with the volume variations can be relieved, accounting for the good cycle performance; and 3) The existence of Cu particle in Cu-Cu<sub>2</sub>O hybrid architectures enhances electronic conductivity and has a catalytic effect for the decomposition of Li<sub>2</sub>O.<sup>40</sup>

## Conclusions

In conclusion, Cu-Cu<sub>2</sub>O hybrid architectures were prepared via a facile one-pot solution method. The controlled over-reduction of Cu(II) under the strong alkaline condition yielded truncated monodisperse Cu<sub>2</sub>O cubes, uniform Cu-Cu<sub>2</sub>O hybrid architectures, irregular Cu<sub>2</sub>O crystals, through a sequential reduction, caramelization of glucose, and oxidation process. Along with the over-reduction of Cu-Cu dimers in the {100} surfaces of truncated Cu<sub>2</sub>O cubes, the metallic Cu particles grew on the corner and edge surfaces, resulting in the novel Cu-Cu<sub>2</sub>O concave cubes hybrid architectures. The Cu-Cu<sub>2</sub>O hybrid architectures exhibited superior electrochemical performance for lithium-ion batteries to the truncated Cu<sub>2</sub>O cubes and irregular Cu<sub>2</sub>O crystals. The concave hybrid structures can play an important role in the intercalation and deintercalation of Li ions, and the metallic Cu component leads to an enhanced

electronic conductivity and a catalytic effect which facilitates the decomposition of SEI layer, thereby improving the performance of lithium-ion batteries

## Acknowledgements

The Project Sponsored by the Scientific Research Foundation for the Returned Overseas Chinese Scholars, State Education Ministry. This work was also financially supported by National Basic Research Program of China (973 Program) (2013CB632405), the National Natural Science Foundation of China (NSFC, Grant No. 21273038), and the Fund of Key Laboratory of Optoelectronic Materials Chemistry and Physics, Chinese Academy of Sciences (2008DP173016). This work was also supported by Japan Science and Technology Agency (JST), PREST in Japan.

## Notes and references

<sup>a</sup> Research Institute of Photocatalysis, State Key Laboratory of Photocatalysis on Energy and Environment, Fuzhou University, Fuzhou 350002, China. E-mail: qiuxq@fzu.edu.cn; Fax: +86-591-83969021; Tel: +86-591-83966021.

<sup>b</sup> State Key Laboratory Cultivation Base for Nonmetal Composites and Functional Materials, Southwest University of Science and Technology, Mianyang 621010, China.

<sup>c</sup> Department of Metallurgy and Ceramic Science, Tokyo Institute of Technology, 2-12-1 Ookayama, Meguro-ku, Tokyo, 152-8552 (Japan). E-mail: mmiyauchi@ceram.titech.ac.jp

† Footnotes should appear here. These might include comments relevant to but not central to the matter under discussion, limited experimental and spectral data, and crystallographic data.

Electronic Supplementary Information (ESI) available: [Details of experimental procedures, characterization methods, XRD patterns, SEM images, discharge-charge curves, and EIS spectra]. See DOI: 10.1039/b000000x/

- 1 T. Mokari, C. G. Sztrum, A. Salant, E. Rabani, U. Banin, *Nat. Mater.*, 2005, **4**, 855-863.
- 2 C. Pacholski, A. Kornowski, H. Weller, *Angew. Chem. Int. Ed.*, 2004, **43**, 4774-4881.
- 3 V. Subramanian, E. E. Wolf, P. V. Kamat, *J. Am. Chem. Soc.*, 2004, **126**, 4943-4950.
- 4 S. W. Jung, W. I. Park, G. C. Yi, M. Y. Kim, *Adv. Mater.*, 2003, **15**, 1358-1361.
- 5 B. P. Khanal, A. Pandey, L. Li, Q. Lin, W. K. Bae, H. Luo, V. I. Klimov, J. M. Pietryga, *ACS Nano*, 2012, **6**, 3832-3840.
- 6 X. Qiu, L. Li, C. Tang, G. Li, *J. Am. Chem. Soc.*, 2007, **129**, 11908-11909.
- 7 X. Qiu, M. Miyauchi, K. Sunada, M. Minoshima, M. Liu, Y. Lu, D. Li, Y. Shimodaira, Y. Hosogi, Y. Kuroda, K. Hashimoto, *ACS Nano*, 2011, **6**, 1609-1618.
- 8 P. Meduri, C. Pendyala, V. Kumar, G. U. Sumanasekera, M. K. Sunkara, *Nano Lett.*, 2009, **9**, 612-616.
- 9 A. L. M. Reddy, S. R. Gowda, M. M. Shaijumon, P. M. Ajayan, *Adv. Mater.* 2012, **24**, 5045-5064.

- 10 H. Zhang, M. Jin, Y. Xiong, B. Lim, Y. Xia, *Acc.Chem. Res.*, 2013, **46**, 1783-1794.
- 11 D. D. Vaughn II, R. E. Schaak, *Chem. Soc. Rev.*, 2013, **42**, 2861-2879.
- 12 J. J. Duan, Y. Zheng, S. Chen, Y. Tang, M. Jaroniec, S. Z. Qiao, *Chem. Commun.*, 2013, **49**, 7705-7707.
- 13 S. Chandren, B. Ohtani, *J. Photochem. Photobio. A*, 2012, **246**, 50-59.
- 14 Y. Liu, A. R. Hight Walker, *J. Phys. Chem. C*, 2010, **114**, 4264-4271.
- 15 M. Leng, M. Liu, Y. Zhang, Z. Wang, C. Yu, X. Yang, H. Zhang, C. Wang, *J. Am. Chem. Soc.*, 2010, **132**, 17084-17087.
- 16 M. Hara, T. Kondo, M. Komoda, S. Ikeda, J. N. Kondo, K. Domen, M. Hara, K. Shinohara, A. Tanaka, *Chem. Commun.*, 1998, 357-358.
- 17 H. Pang, F. Gao, Q. Lu, *Chem. Commun.*, 2009, 1076-1078.
- 18 M. Kevin, W. L. Ong, G. H. Lee, G. W. Ho, *Nanotechnology*, 2011, **22**, 235701.
- 19 B. P. Rai, *Solar Cells*, 1988, **25**, 265-272.
- 20 P. Poizot, S. Laruelle, S. Grugeon, L. Dupont, J. M. Tarascon, *Nature*, 2000, **407**, 496-499.
- 21 L. Gou, C. J. Murphy, *Nano Lett.*, 2002, **3**, 231-234.
- 22 C. Lu, L. Qi, J. Yang, X. Wang, D. Zhang, J. Xie, J. Ma, *Adv. Mater.*, 2005, **17**, 2562-2567.
- 23 J. C. Park, J. Kim, H. Kwon, H. Song, *Adv. Mater.*, 2009, **21**, 803-807.
- 24 Y. Sui, W. Fu, Y. Zeng, H. Yang, Y. Zhang, H. Chen, Y. Li, M. Li, G. Zou, *Angew. Chem. Int. Ed.*, 2010, **49**, 4282-4285.
- 25 N. Meir, I. Jen-La Plante, K. Flomin, E. Chockler, B. Moshofsky, M. Diab, M. Volokh, T. Mokari, *J. Mater. Chem. A*, 2013, **1**, 1763-1769.
- 26 L. Zhang, D. A. Blom, H. Wang, *Chem. Mater.*, 2011, **23**, 4587-4598.
- 27 L. Kong, W. Chen, D. Ma, Y. Yang, S. Liu, S. Huang, *J. Mater. Chem.*, 2012, **22**, 719-724.
- 28 Y. Q. Wang, K. Nikitin, D. W. McComb, *Chem. Phys. Lett.*, 2008, **456**, 202-205.
- 29 C.-H. Kuo, Y.-C. Yang, S. Gwo, M. H. Huang, *J. Am. Chem. Soc.*, 2010, **133**, 1052-1057.
- 30 A. Goyal, A. L. M. Reddy, P. M. Ajayan, *Small*, 2011, **7**, 1709-1713.
- 31 G. Evano, N. Blanchard, M. Toumi, *Chem. Rev.*, 2008, **108**, 3054-3131.
- 32 A. Radi, D. Pradhan, Y. Sohn, K. T. Leung, *ACS Nano*, 2010, **4**, 1553-1560.
- 33 N. Li, Y. Xiao, C. Hu, M. Cao, *Chem-Asian J.*, 2013, **8**, 1960-1965.
- 34 J. Dai, X. M. Fan, H. Liu, J. Wang, H. R. Liu, F. Z. Zhang, *J. Nanosci. Nanotechno.*, 2012, **12**, 6412-6419.
- 35 A.-J. Wang, J.-J. Feng, Z.-H. Li, Q.-C. Liao, Z.-Z. Wang, J.-R. Chen, *CrystEngComm*, 2012, **14**, 1289-1295.
- 36 J. Kou, A. Saha, C. Bennett-Stamper, R. S. Varma, *Chem. Commun.*, 2012, **48**, 5862-5864.
- 37 M. Casavola, V. Grillo, E. Carlino, C. Giannini, F. Gozzo, E. Fernandez Pinel, M. A. Garcia, L. Manna, R. Cingolani, P. D. Cozzoli, *Nano Lett.*, 2007, **7**, 1386-1395.
- 38 C.-H. Kuo, M. H. Huang, *J. Am. Chem. Soc.*, 2008, **130**, 12815-12820.
- 39 Z. Yang, S. Sun, C. Kong, X. Song, B. Ding, *J. Nanomater.*, 2010, **2010**, 710584.
- 40 J. Y. Xiang, J. P. Tu, Y. F. Yuan, X. H. Huang, Y. Zhou, L. Zhang, *Electrochem. Commun.*, 2009, **11**, 262-265.
- 41 X. Qiu, M. Liu, K. Sunada, M. Miyauchi, K. Hashimoto, *Chem. Commun.*, 2012, **48**, 7365-7367.
- 42 W. G. Berl, C. E. Feazel, *J. Agric. Food Chem.*, 1954, **2**, 37-39.
- 43 V. Fogliano, S. Maria Monti, T. Musella, G. Randazzo, A. Ritieni, *Food Chem.*, 1999, **66**, 293-299.
- 44 C. Billaud, E. Roux, S. Brun-Mérimee, C. Maraschin, J. Nicolas, *Food Chem.*, 2003, **81**, 35-50.
- 45 Z. Fang, R. L. Smith Jr, J. A. Kozinski, T. Minowa, K. Arai, *J. Supercrit. Fluids* 2011, **56**, 41-47.
- 46 B. Jiang, Y. Liu, B. Bhandari, W. Zhou, *J. Agric. Food Chem.*, 2008, **56**, 5138-5147.
- 47 T. Ing, X. Zhou, A. Yu, N. Vaziru, *Periton. Dialysis Int.*, 1992, **12**, 276-277.
- 48 A. Soon, M. Todorova, B. Delley, C. Stampfl, *Phys. Rev. B*, 2007, **75**, 125420.
- 49 Y. Feng, K. S. Siow, W. K. Teo, K. L. Tan, A. K. Hsieh, *Corrosion*, 1997, **53**, 389-398.
- 50 X. Guan, L. Li, G. Li, Z. Fu, J. Zheng, T. Yan, *J. Alloys Compd.*, 2011, **509**, 3367-3374.
- 51 P. G. Bruce, S. A. Freunberger, L. J. Hardwick, J.-M. Tarascon, *Nat. Mater.*, 2012, **11**, 19-29.
- 52 A. L. M. Reddy, M. M. Shaijumon, S. R. Gowda, P. M. Ajayan, *Nano Lett.*, 2009, **9**, 1002-1006.
- 53 Q. Pan, M. Wang, *J. Electrochem. Soc.*, 2008, **155**, A452-A456.
- 54 X. H. Huang, J. P. Tu, C. Q. Zhang, J. Y. Xiang, *Electrochem. Commun.*, 2007, **9**, 1180-1184.